

Aboveground biomass estimates from UAV LiDAR improved via contextual learning in a Norway spruce forest

Jaime C. Revenga^{1,3} | Stefan Oehmcke² | Mana Gharun³ | Flurin Sutter⁵ | Fabian Gieseke² | Katerina Trepekli¹ | Nina Buchmann⁶ | Alexander Damm^{7,8}

¹Department of Biology, Ecoinformatics and Biodiversity, Aarhus University, Denmark.

²Institute of Computer Science, University of Copenhagen, Denmark

³Institute of Geosciences and Natural Resources Management, University of Copenhagen, Denmark.

⁴Institute of Landscape Ecology, Biosphere-Atmosphere Interaction, University of Münster, Germany.

⁵Swiss Federal Institute for Forest, Snow and Landscape Research, Forest Dynamics Research Unit, Switzerland.

⁶Department of Environmental Systems Science, ETH Zürich, Switzerland.

⁷Department of Geography, University of Zürich, Winterthurerstrasse 190, 8057 Zurich, Switzerland.

⁸Eawag, Swiss Federal Institute of Aquatic Science & Technology, Surface Waters – Research and Management, Ueberlandstrasse 133, 8600 Dübendorf, Switzerland.

Correspondence

Jaime C. Revenga, Øster Voldgade 10, 1350, København, Denmark.
Email: jar@ign.ku.dk

Forest structure and aboveground biomass (AGB) analyses are key for advancing forest trait-based ecology and management. Surveys using Unmanned Aerial Vehicles (UAV) and Light Detection and Ranging (LiDAR) systems have contributed to this field with increased accuracy in tree phenotyping. Moreover, methods harnessing the flexibility of machine learning (ML) are now common tools to enhance estimates of AGB. Here, we evaluated the capacity of shallow learning methods to leverage local information from the surrounding context of the tree of interest to improve predictions of stem diameter and tree-level biomass, over 33 ha of a Norway spruce forest (Davos, CH). Our objectives have been (i) to gain insights into variation and gradients of tree heights and (ii) to evaluate whether such gradients may prove useful as contextual information to improve predictions. We segmented the point cloud data scene into individual canopies and focused the LiDAR-derived tree canopy features. We then used local indicators of spatial association to determine the influence of local context on tree height, and used this to define tree neighborhoods within

the forest. Then, we extracted metrics from the neighborhoods and introduced them in a ML regression experiment to evaluate predictions of individual tree diameter. The focus was on comparing performance of tree diameter predictions between twin regression models that either consider neighborhood metrics (i.e. context-aware models), or not. Then, the improvements provided by context awareness were assessed in terms of accuracy gained in estimating AGB. We obtained results of three different shallow learning methods and evaluated these based on nested cross-validation. We applied this approach to two separate data sets within the same site, one being clustered and continuous; the other discontinuous and scattered in separate sampling plots. In both cases, we found enhanced AGB prediction performance in context-aware regressions, where the RMSE was reduced by 4.0% and by 9.1%, respectively. These findings indicate that gradients in tree heights across the ecosystem may proxy for local microclimate, edaphic conditions and biotic factors that influence tree growth, which can be leveraged to enhance predictions of AGB. The method proposed is fully native to UAV LiDAR data.

KEYWORDS

aboveground biomass, UAV LiDAR, forest structure, functional trait mapping, machine learning, contextual learning, quantitative ecology

Code and/or data are made available for peer review, uploaded as separate files for reviewers and editors.

1 | INTRODUCTION

Forest aboveground biomass (AGB) is an important component in determining global carbon budgets (C), and they are considered essential to understand the exchange of C between the atmosphere and the biosphere [1, 2]. A large body of environmental remote sensing research has advanced our understanding of it. However, current assessments of C-cycling in forest ecosystems present uncertainties, and contrasting findings exist [3], partly caused by the limited accuracy of AGB estimates [4, 5]. This underscores the need to advance methods to improve quantitative estimates of forest AGB [6] from remotely sensed data.

Predictive analyses in forest AGB and phenotyping from remote sensing surveys have traditionally been focused

56 on regressions considering only individual tree attributes as predictors (e.g. tree height, canopy metrics) [7, 8] and
57 fitted allometric models [9]. Such tree-level analyses have been crucial to improve the characterization of e.g. optical
58 vegetation traits [10], tree dendrometry [11], or species composition [12]. However, these approaches generally do
59 not account for the influence of the spatial context on the individual tree trait under investigation, be it abiotic factors
60 (e.g. terrain condition, soil depth) or biotic interactions (e.g., light interception, nutrient competition), although it is
61 established knowledge that the local context (microclimatic, edaphic and biotic conditions) condition tree traits. In
62 this regard, the mixed effect of abiotic conditions and biotic interactions on individual tree performance has been
63 long hypothesized [13, 14]. Moreover, a line of empirical research has aimed to measure tree performance compo-
64 nents (e.g. stature, dominance) across environmental gradients, while monitoring local biotic interactions [15]. Indeed,
65 an increasing number of empirical studies, have proposed different methods to use the information of neighboring
66 trees to enhance individual tree trait regressions (i.e. metrics derived from monitoring inventory plots), such as non-
67 linear mixed effects (NLME) methods [16, 17, 18], or competition-based methods [19, 20, 21]. This line of research
68 has shown that considering neighborhood information can improve trait estimates, and its positive impact has been
69 documented in various tree-level regression analyses, e.g. productivity [22, 23], fuel potential [24] or structural met-
70 rics [18, 25, 26].

71

72 However, despite the utility of current methods that leverage neighborhood metrics such as tree stand informa-
73 tion, from a remote sensing perspective they result suboptimal in some respects. Many of such methods are not
74 directly transferable to a remote sensing framework because they use understory metrics as predictors (e.g. stem
75 diameter of neighboring trees), which are difficult to survey reliably from an above-canopy perspective [19, 20]. Addi-
76 tionally, questions remain about the optimal scale at which such neighborhood metrics become relevant and therefore
77 should be retrieved [22, 23]. A common procedure is to consider the trees contained in an arbitrarily delineated inven-
78 tory plot, whose size is defined to fit management purposes [23]. This approach, although useful for monitoring tasks,
79 can pose the shortcoming of overlooking the spatial scale at which relevant ecological phenomena operate (e.g. the
80 appropriate range at which tree competition effects are significant), so the analysis remains constrained by the effects
81 observed at the scale of the plot size [16, 17, 18, 19, 20]. To the best of our knowledge, tree-level AGB and trait as-
82 sessments considering neighborhood information are currently limited due to one or more of the following reasons: (i)
83 they characterize the spatial context with uniquely process-specific indices (e.g. competition pressure from immediate
84 neighbors) [19, 20, 21]; (ii) they calibrate models with neighborhood-metrics retrieved from artificially-bounded inven-
85 tory plots (e.g. NLME methods) [16, 17, 18]; or (iii) they overlook the spatial scale at which an ecological phenomenon
86 affects the trait under investigation. Moreover, when the relationship between the plot-level predictors used and any
87 ecological phenomenon is described, often ancillary data sources are incorporated (e.g. tree stand age) [20, 27] or
88 roughly quantified forest management metrics, e.g. "stand quality", "site index", "dominance index" [17, 20, 27]. These
89 shortcomings are constrained by the specific data collection protocol, and currently hinder transferring such methods
90 to an integrated remote sensing framework, which would offer greater flexibility for conducting standardized, scalable,
91 and replicable forest analyses.

92

93 Unstaffed Aerial Vehicles (UAV) equipped with Light Detection and Ranging (LiDAR) monitoring systems are re-
94 garded as particularly versatile [28], accurate and cost-effective tools [29] to contribute to the task of extensive
95 phenotyping, bridging scales in AGB mapping, particularly covering the scale between *in situ* field-based inventories
96 (approx. 0-1 ha) and airborne LiDAR datasets (approx. 1-10⁴ km²) [30, 31]. With a surveying accuracy comparable to
97 field-based measurements, UAV LiDAR monitoring provides datasets (i.e. point cloud data, PCD) that allow individual
98 tree phenotyping at an intermediate spatial scale (approx. 1-40 ha).

99

100 While it is commonly argued that understanding local ecological processes in forests requires monitoring biomass
101 of individual trees [20, 22, 23, 32], the opposite idea is seldom discussed: how and to what extent can community ecol-
102 ogy processes be harnessed in tree-level AGB regression experiments? Earlier works have proposed to account for the
103 effects of immediate competition pressure on tree growth with either distance-based [21] or distance-independent
104 metrics [19, 33], generally finding such approaches beneficial to improve regression results [19, 20]. However, these
105 studies are based on the premise that competition indices are the determining factor conditioning tree development,
106 while overlooking other potential regulation factors. In this scenario, nonparametric ML regression methods, which
107 do not assume preexisting distributions or premises, are a sound approach to incorporate a contextual analysis, and
108 have been proposed in previous forest mapping studies [34].

109

110 Context-based regression studies [35, 36] have shown in the last decade that the inclusion of information of lo-
111 cal context (i.e. information about the surroundings of the target object) may improve model performance [37, 38].
112 This information can be included in a learning model by either enlarging the receptive field size (i.e. widening the
113 field of view) [34, 38, 39] or by incorporating context-aware features that encode neighboring information into the
114 target object [40] (i.e. a specific tree in forestry applications). However, context-based studies typically rely on deep
115 learning architectures and large datasets [34], which may obfuscate the explainability of model performance improve-
116 ment, which make them suboptimal for ecological applications, where the focus is on explaining regulation factors. In
117 contrast, when interpretability and dataset size limitations are critical, shallow learning methods (e.g. ensembles of
118 decision trees and regularized linear models) are preferred [41, 42].

119

120 Here, we developed a fully integrated UAV LiDAR framework to provide context information into regression ex-
121 periments to predict tree-level AGB, over 33 ha of a Norway spruce forest. We did so only using shallow learners
122 to maintain the focus on the context regulation factors on tree-level AGB (which are ecosystem-dependent), instead
123 of on the specific model architecture (which is ecosystem-independent). Moreover, the method we present is inde-
124 pendent of ancillary data sources and metrics obtained from artificially bounded inventory plots. To that end, we i)
125 collected close-range PCD via UAV LiDAR surveying in a Norway spruce forest, ii) retrieved contextual information
126 based on the geographic spatial association of tree heights, iii) integrated context into pairs of twin regression exper-
127 iments (i.e. identical except on the fact of context), and iv) evaluated the effect of introducing context-awareness in
128 tree-level AGB estimates. The findings show that the prediction enhancement caused by including context-awareness,
129 is robust across three different shallow learning methods for two separate datasets within the same coniferous forest.
130 The proposed method is conceived to not rely on additional data sources beyond the UAV LiDAR datasets, in order
131 to ease applicability.

132

133 2 | MATERIALS AND METHODS

134 2.1 | Study Area

135 The Seehornwald Davos research site (46° 48' 55.2"N, 9° 51' 21.3" E, 1640 m a.s.l.) is located in a managed subalpine
136 coniferous forest on the western flank of the Seehorn mountain, near Davos, in the Swiss Alps. The site is labeled
137 as a class-1 forest ecosystem station of the Integrated Carbon Ecosystem Station (ICOS) network [43] where regular
138 forest inventory measurements are collected following standardized protocols. The site is covered by spruce trees

139 (*Picea abies* (L.) Karst., > 99.5 %) with an average height and age of 14 m and 100 years, respectively, while some trees
 140 reach a height of 40 m and an age of 300 years. The stand parameters at the research site include tree density: 639
 141 \pm 311 tree/ha; basal area: 27.6 ± 16 m²/ha; mean crown area of dominant canopy: 13.2 m²; and mean DBH: 17.7 cm.

142 The site has not been affected by infrastructure development during the 20th-21st centuries. Since 1930, grazing
 143 livestock in the forest was abandoned, and the site is sustainably managed according to the Swiss Forest Law (1876,
 144 revised until 2017) [44]. Maps dating back to 1845 reveal minimal changes within the Davos-Seehornwald forest
 145 site, while slight effects of local harvests are noticeable, particularly on steeper slopes of the eastern flank, and forest
 146 regrowth at the timberline can also be observed [45]. Patchy vegetation (i.e. dwarf shrubs and mosses) covers around
 147 30% of the forest floor (acidic ferralic podzols), which lies on a mixed silicious and dolomitic bedrock. The research site
 148 is part of national (LWF [46], TreeNet [47], SwissFluxNet [48]) and international research networks (ICOS [49], ICP
 149 Forests [50], eLTER [51]). The study area spans over 33 ha (Figure 1, b) and the terrain conditions are representative
 150 of the Alps around the Landwasser valley, i.e. a varying steepness of $23 \pm 14^\circ$. The site lies on the eastern flank of
 151 the valley, so most of the slopes face west-southwest (mean slope aspect is 230° SW).

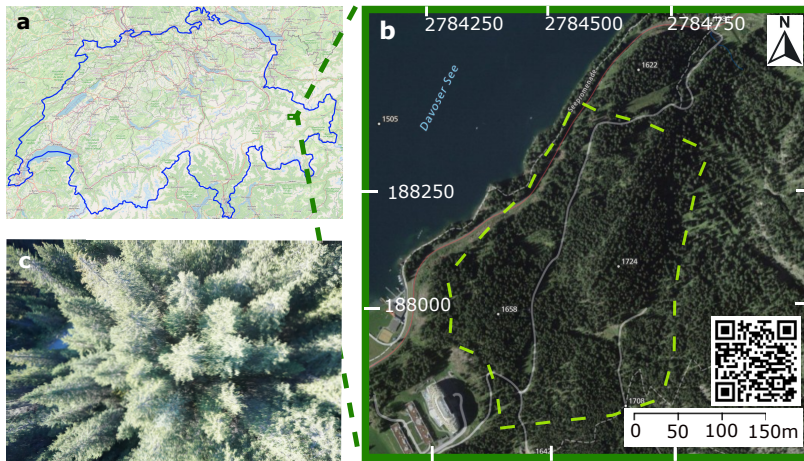


FIGURE 1 a: Location of the study site; the blue outline delineates the national territory of Switzerland (adapted from open.sourcemap.com). b: Orthoimage of the study site (adapted from swisstopo.admin.ch); coordinate units are in m, with LV95 as a projected reference system; the QR code links to additional information of the study site. The dashed yellow line shows the boundaries of the research site. c: Ortophoto of the study site.

152 2.2 | UAV LiDAR Survey and Field-Based Measurements

153 We used a UAV-borne LiDAR system mounted to a DJI Matrice 600 Pro payload at a 90° pitch angle, and same head-
 154 ing and roll as the UAV platform. The system included a discrete infrared LiDAR scanner (M8 sensor, Quanenergy
 155 Systems, Inc. Sunyvale, CA, USA) and the corresponding state-of-the art inertial and navigation systems. In addition,
 156 we used a ground based Global Navigation Satellite System (GNSS, Trimble R8) during the UAV LiDAR survey, set up
 157 in post-positioning kinematic (PPK) mode, which logged real-time satellite coverage (cf. Revena et al. 2022 [52] for
 158 details on the airborne and ground system). The coupling of the satellite coverage data with the UAV-based laser and
 159 navigation data produced, allowed the generation of georeferenced point clouds, following Davidson et al. (2019) [53].

160

161 Data were acquired with a UAV flight height adapted to the terrain and tree height (Figure 2, a), ensuring a >20%
 162 overlap between individual LiDAR scans of approx. 50 m width and 250 points/m². The surveys were conducted in
 163 October 2021, coinciding with the end of the forest growing season. Figure 2 (a) shows the trajectories of the UAV Li-
 164 DAR flights during the survey campaign. While the standard survey coverage followed a regular auto-pilot flight grid,
 165 certain flight lines had to be manually piloted to adapt to sudden topographic features and canopy structure. The
 166 digital elevation model of the study area is provided in Annex VI, to help to understand differences in flight heights.
 167

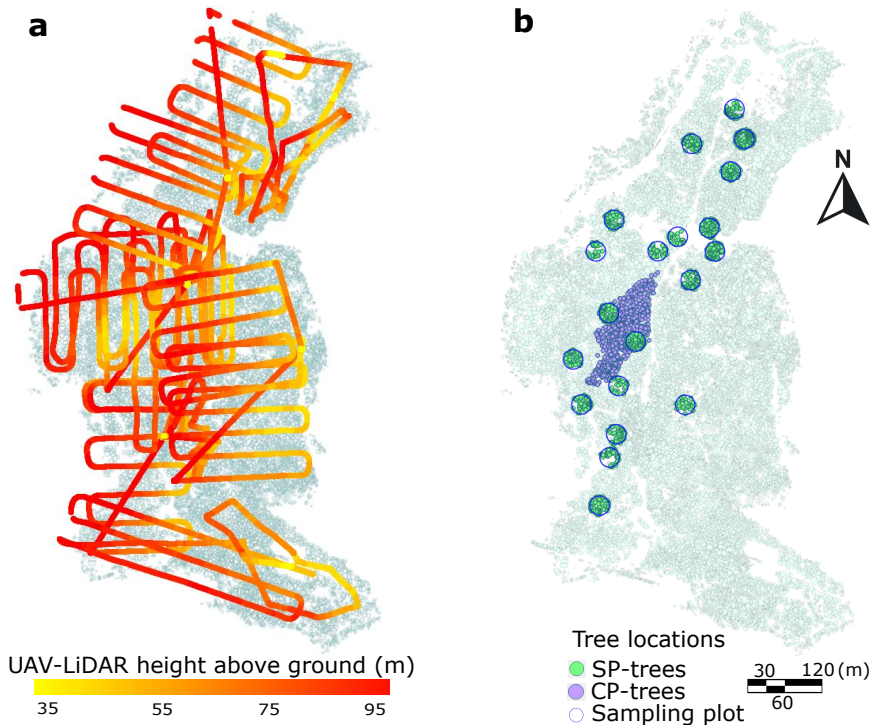


FIGURE 2 a: Trajectories of individual flights during survey of the Unstaffed Aerial Vehicle (UAV) Light Detection and Ranging (LiDAR) sensor; color gradient indicates height above ground during survey. Only the trajectories during LiDAR data acquisition are shown (take off and landing trajectories not shown); the variable height corresponds to the difference between a horizontally stable UAV survey and the variable terrain elevation. b: Spatial distribution of field-based forest inventory. Dots represent the locations of the ground truth labels. The sampling plot-trees (SP-trees, N = 1635 trees) are shown in green; the control plot-trees (CP-trees, N = 845 trees) are shown in purple. In both a and b, the underlying polygon dataset shows the individual tree canopies after the canopy height model segmentation.

168 The field-based measurements (shown in Figure 2, b) are taken on a yearly basis as part of a long-term ecosystem
 169 monitoring initiative—jointly organized by ICOS [49] and the Swiss Federal Institute for Forest, Snow and Landscape
 170 Research (WSL) [46]. Following a standardized protocol [54], expert field workers monitor tree crown status, focusing
 171 on three groups of indicators: variations in size, density and color. The number of trees that have died since the previ-
 172 ous survey, as well as the new ones that reached a minimum DBH of 5 cm are also recorded [55]. Tree height and DBH
 173 are monitored with a high-precision digital rangefinder (i.e. Vertex Laser Geo) and a standard calliper, respectively.

We treated two different datasets separately as ground truth measurements within the same study area: control plot trees (CP-trees, 4 adjacent monitoring units) and sampling plot trees (SP-trees, 20 scattered units of 15 m radius). The two datasets (i.e. CP- and SP-trees) are monitored by different research groups on the field and protocols presented minor differences between both datasets. Two main factors led us to consider both datasets separately: (i) the CP-dataset is clustered and spatially continuous, while the SP-dataset is spatially discontinuous and distributed along the study site (Figure 2, b); and (ii) the two datasets present differences in morphological trait distribution (Annex V). Figure 2 (b) shows the spatial distribution of the field-based forest inventory. The CP tree position was recorded using a Leica GPS1200 total station. The location and size of the sampling plots were defined according to ICOS protocols [56]. The center location of the SP plots was determined using a GNSS Leica CS20 (antenna GS15) with a real-time kinematic (RTK) signal (accuracy measurements ranges from 0.03 m to 0.7 m). Next, the trees in the SP plots were positioned by measuring the azimuth with a field goniometer, while the horizontal distance of each tree and the inclination from the plot centers was determined using a Vertex Laser Geo meter. The accuracy of foot location of trees in the SP plots is within 0.5m and 1.2 m. The field-based inventories used as ground truth contain measurements taken between October 2019 and July 2021. The changes in structural traits of max. two years between field-based measurements and UAV LiDAR data acquisition were considered negligible for the purposes of this study and no major disturbance events were registered during this period.

2.3 | Method setup

The workflow followed in this study is presented in Figure 3. Initially, the PCD generation followed the approach described in Revenga et al. (2022) [52]. The resulting PCD scene was normalized and rasterized to obtain a canopy height model (CHM), which in turn was subject to individual tree crown segmentation producing a two-dimensional polygon dataset. For the CHM segmentation, we utilized a watershed algorithm specifically designed for coniferous forests [57]. The match between field-based measurements and individual tree crown (ITC) polygons was conducted based on the closest distance between the field-based GNSS point measurement and the ITC polygon centroid.

In order to ensure that only the LiDAR-detected trees would be accounted for in the regression experiment, a pre-processing task was required (marked * in Figure 3, the details of the preprocessing tasks involved are given in Annex II). Afterwards, using the LiDAR-derived height as polygon attribute, we calculated the distance at which the spatial autocorrelation of tree height was most significant in order to define the optimal neighborhood size (as explained in Section 3.1). Once the optimal neighborhood size had been defined, we conducted the local indicators of spatial association (LISA) analysis [58, 59] and outlier analysis [60, 61] to retrieve neighborhood metrics. Finally, two separate supervised regression experiments were performed, in order to predict DBH based on LiDAR-derived metrics: one including the neighborhood metrics (context-aware regression), the other without taking those metrics into account (context-unaware regression). Finally, AGB was estimated from the predicted DBH via an allometric function (as defined in Eq. 5).

Finally, we conducted a second task to characterize the morphometry of tree assemblages (i.e. groups of adjacent trees fulfilling a specific criterion of height similarity, as explained in Section 2.3) stemming from the ITC polygon dataset. Prior to the morphometric analysis of tree assemblages, a second pre-processing task was conducted (details are given in Annex II).

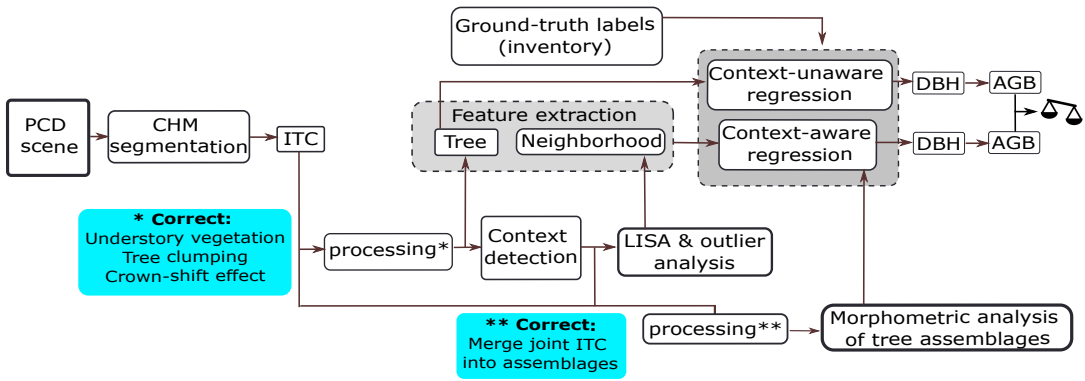


FIGURE 3 Workflow followed in this study. PCD: point cloud data, CHM: canopy height model, ITC: individual tree crown, LISA: local indicators of spatial association, DBH: diameter at breast-height, AGB: aboveground biomass. The two blue boxes describe the subtasks constituting each of the processing steps, marked * and ** in the diagram.

214 | Definition of Context Via Tree Heights in the Neighborhood

215 We determined the distance at which neighborhood metrics should be calculated (i.e. how many surrounding trees
 216 should be accounted as neighbors) based on local similarity of tree height. Accordingly, the selection of an appropriate
 217 neighborhood size around each individual tree (i.e. context detection) [62] was calculated through the analysis of spa-
 218 tial autocorrelation of tree height as function of incremental distance, as in previous studies [63]. Based on the global
 219 peak in the significance of spatial autocorrelation, we defined a characteristic distance within which all included trees
 220 should be considered as neighbors. Then, all so-defined neighbor trees were accounted for to compute context-aware
 221 metrics.

222
 223 The local context information was encoded as metrics derived from the distance-weighted individual tree heights
 224 in each neighborhood, calculated at each tree location. Specifically, the metrics computed to define the local context
 225 were: local Moran's I [58] (i.e. an estimate of local significance of tree height similarity with respect to the global
 226 variance); and (SL_i) of tree height (i.e. a weighted average of heights calculated entirely locally) [64].

227
 228 Local Moran's I_i is a well-established distance statistic in spatial data analysis [65], used for detecting local spatial
 229 autocorrelation and included within the family of LISA methods [58, 59, 64]. Similarly to other geostatistics meth-
 230 ods [66], it relates attribute similarity with locational similarity, mapping autocorrelation across the geographic space.
 231 In the following definitions, σ is the global sample standard deviation of tree height; n and m represent the total num-
 232 ber of instances (i.e. all trees in the forest) and the number of neighbors to each tree, respectively; y_i indicates the
 233 magnitude of interest at a particular point of interest (i.e. tree height) while the overline (i.e. \bar{y}) indicates the global
 234 average; $w_{i,j}$ indicates the distance weighting of each neighboring tree (here defined as inverse distance weighting);
 235 subindexes i and j indicate the tree of interest and a neighbor tree, respectively. Let y_1, \dots, y_n be the tree height
 236 values of all the n trees in the dataset. Then, the Local Moran's I_i [58] is defined as

$$I_i = \frac{y_i - \bar{y}}{\sigma^2} \sum_{j \in N_i, j \neq i} w_{i,j} (y_j - \bar{y}), \quad (1)$$

237 where $N_i \subset \{1, \dots, n\}$ is the set of indices corresponding to the nearest neighbors of tree $i \in \{1, \dots, n\}$ in the
 238 overall set, where

$$\bar{y} = \frac{1}{n} \sum_{i=1}^n y_i, \quad (2)$$

239 and

$$\sigma = \sqrt{\frac{\sum_{i=1}^n (y_i - \bar{y})^2}{n - 1}}, \quad (3)$$

240 are the global average height and the global sample standard deviation, respectively. It should be noted that
 241 insofar I_i includes global metrics (such as n , σ and \bar{y}), it is not entirely locally computed, but may present correlation
 242 with global features (i.e. characteristics derived from the entire dataset; cf. Westerholt et al. 2018) [67].

243 The Spatial Lag (SL_i) of tree height for a tree i is a spatial smoother [68] defined as

$$SL_i = \sum_{j \in N_i, j \neq i} w_{i,j} y_j \quad (4)$$

244 where the elements of the spatial weights matrix ($w_{i,j}$) are row-standardized, so that $\sum_{j \in N_i, j \neq i} w_{i,j} = 1$. Therefore,
 245 SL_i can be seen as a weighted average of the heights of neighboring trees [69].

246
 247 The neighborhood metrics finally chosen as context-aware predictors are the following: local Moran's Index (I_i),
 248 z-score of I_i , p-value of I_i , z-transformed value of I_i and SL_i —computed at 20 m, 30 m, 40 m and 50 m distance bands.
 249 Additionally, the mean heights of the k-nearest trees, with $k \in (5 - 75)$, were also included as predictors. Likewise,
 250 we also included the topographic wetness index (TWI) [70] in order to evaluate the relative predictive performance of
 251 neighborhood metrics with respect to a well-established environmental variable as tree-growth predictor [71] (details
 252 are given in Annex VII).

253 Finally, we included in the regression experiments predictive features informing of local neighbor dissimilarity,
 254 i.e. local outliers of tree height. We detected local outliers using Local Outlier Factor [60] and Isolation Forest [61]
 255 algorithms. The evaluation of these features allowed us to discern between the contribution of local similarity features
 256 (i.e. Local Moran's I_i and SL_i) and that of the local outliers.

257 | Tree Assemblages' Morphometry

258 In order to define the tree assemblages, both local Moran's I_i and SL_i were computed at the optimal distance band to
 259 obtain neighborhood metrics, i.e. based on the global peak in the significance of spatial autocorrelation of tree height
 260 as a function of distance (using ArcGIS Pro) [72].

261
 262 Tree assemblages were therefore defined as geographically continuous groups of trees delineated according to
 263 either (i) variation of local Moran's I_i of tree height, or (ii) according to quantiles of SL_i of tree height. The rationale
 264 for using two different statistics to calculate tree neighborhood metrics and thus delineate different tree assemblages

265 was that while SL_i is entirely locally calculated, local Moran's I_i includes global features (and is therefore sensitive to
266 the statistical characteristics of the dataset as a whole), as explained in Section 2.3. In order to discern which of the
267 two approaches resulted most convenient in delineating tree assemblages (the former *entirely* local; the latter only
268 *partially* local), both were included.

269
270 Tree assemblages defined according to local Moran's I_i are geographically continuous groups of trees with signif-
271 icantly different heights than the global tree height average, and they also lie in a region with significantly different
272 neighbors. Local Moran's I_i identifies regions where the clustering of either high or short trees occurs. In the standard
273 notation [64] (i.e. *High-High* or *Low-Low*), the first term refers to the individual tree and the second to the neighborhood
274 (e.g. a tree belonging to a *High-High* assemblage is a "significantly high tree" in a "significantly high neighborhood"). The
275 areas not showing statistical significance (a p-value ≥ 0.002 was considered sufficient) were labeled as *Not-Significant*.
276 The significance test is based on random permutations ($n = 499$) of neighboring tree-height values at each step in the
277 computation. The number of permutations and p-value indicate that, under the null hypothesis (i.e. tree heights being
278 randomly distributed), a single tree canopy is likely to be wrongly classified with a probability of 0.002, which was
279 deemed sufficient for the purpose of evaluating tree assemblage morphometry (i.e. if 1 out of 499 trees is wrongly
280 attributed to a neighborhood, the morphometry of the assemblage will not change markedly). Then, for every permu-
281 tation, a local Moran's I_i value was calculated by randomly rearranging the tree heights of neighboring values. The
282 result is a randomly generated reference distribution of expected local Moran's I_i that is compared against the ob-
283 served local Moran's I_i (Eq. 1) [59]. In this way, tree assemblages defined according to local Moran's I_i are classified
284 as: *High-High*, *Low-Low*, or *Not-Significant*.

285
286 Likewise, tree assemblages defined according to SL_i of tree height are geographically continuous groups of trees
287 delimited according to the local weighted average of tree height [69], as defined above (Eq. 4). For the purpose of
288 this study, 5 subdivisions based on quantiles were deemed convenient, rendering a classification of tree assemblages
289 based on SL_i ranking as: *Highest*, *High*, *Mid*, *Low* and *Lowest*.

290
291 The morphometric analysis examined the outer boundaries of the tree assemblages as defined above. Twenty
292 basic morphometric parameters as well as 20 derived parameters were calculated for each type of tree assemblage.
293 The 20 basic morphometric variables are simple parameters obtained by fitting elemental geometric shapes to each
294 tree assemblage polygon (e.g. area of maximum inscribed circle), and basic positional parameters (e.g. XPOL, which is
295 the X coordinate of the centroid of the tree assemblage polygon). The 20 derived parameters are adimensional metrics
296 (except for concavity [73], measured in m) computed from the 20 basic morphometric variables, as explained in Güler
297 et al. 2021, [74] (details are given in Annex III). The morphometric analysis of tree assemblages was conducted us-
298 ing PolyMorph-2D algorithm [74], which is a toolbox for the morphometric analysis of vector-based polygon objects,
299 available as a plug-in for the open source JumpGIS software [75].

301 | Regression Models Selected

302 The regression experiments were designed to predict DBH, since AGB is a variable determined by the combination
303 of DBH, height and wood density [9]. Instead, DBH is directly measured in the field, which makes it a better defined
304 regression target. Therefore, the model estimates of AGB were derived from the DBH prediction outputs by means of
305 an allometric fit (Eq. 5). Predicting DBH, instead of AGB directly was chosen as more suitable, as it avoids burdening

the learning models with the statistical error contained in the allometric fit. Three feature-based shallow learning regression methods were selected: namely AdaBoost [76, 77, 78], Lasso [79] and Random Forest [80] regressors. The AdaBoost regressor is a tree-based gradient-boosting method that relies on stage-wise additive expansions. Its effectiveness stems from combining weak learners to form a generalized prediction hypothesis. Random Forest is a well established tree-based ensemble regression method. Finally, Lasso, on the other hand, is a linear model with an $L1$ prior penalty acting as a regularizer [81]. In our case, all three shallow regression methods utilize the features derived from the ITC polygon dataset resulting from the CHM segmentation.

Context-unaware regressions were defined as those in which a learning model performs DBH regression by taking as predictors only individual tree attributes derived from the ITC polygon dataset (i.e. tree height, canopy area and canopy perimeter), as it is a common approach [8]. On the other hand, we defined context-aware regressions as those regressions in which context-aware features are additionally introduced as input in the predicting feature space. These were either neighborhood metrics, e.g. SL_i of tree height, or TWI at different spatial resolutions (Section 2.3). For every model predicting DBH from individual tree attributes (i.e. context-unaware conditions) we implemented a context-aware counterpart. This allowed us to evaluate the impact of context on regression model performance.

Model Training and Validation of Results

A hard validation of AGB is not possible without harvesting trees destructively, which raises obvious ethical, legal and economic issues. Instead, non-invasive methods that use remote sensing data and allometric functions are the standard procedure for estimating AGB [82]. Here, we estimated AGB from tree height, DBH, wood density and an allometric function Norway spruce trees (eq. 5). Therefore, the regression analyses conducted focused on comparing performance of predictions on DBH between twin shallow learning methods (i) "context-unaware" and their (ii) "context-aware" counterparts.

We chose DBH as the variable to test model predictions, which is a tree morphological trait contained in the field-based forest inventory, and therefore directly measured by *in situ* monitoring. Next, in order to assess the benefits of including context in the regression models, we compared results using AGB of individual trees. Specifically, AGB estimates were derived via species-specific allometric and wood density functions, tree height retrieved via UAV LiDAR, and DBH predicted via ML regression. Specifically, the allometric model used was the one proposed by Dalponte and Coomes (2016) [9]:

$$AGB_{tree} = \alpha \cdot WD_{spruce}^{\beta} \cdot (DBH - d_0)^{\gamma} \cdot H^{\delta}, \quad (5)$$

where the wood density value (WD_{spruce}) was taken from Alpine spruce dendrometric models [83], DBH was predicted via ML regression and height (H) was extracted from the UAV LiDAR data. $\alpha, \beta, \gamma, \delta$ and d_0 are species-specific fitted allometric parameters [84], obtained from allometric fits to harvested spruce trees by the Forestry and Wildlife Service Agency of the province of Trento (an Italian neighbouring province southeast from the study site, also used in Dalponte and Coomes, 2016) [9], and we consider them applicable to the Seehornwald Davos research site. At all events, for the purpose of assessing the benefits of a context-aware approach, the specific characteristics of the allometric fit used are negligible, as it is only used to quantify a difference in terms of AGB, and both types of

343 predictions (unaware and aware) take the same equation. Therefore, the predicted value of DBH (in either aware or
344 unaware conditions) was input into Eq. 5, in order to obtain model predictions of AGB. This allowed to compare AGB
345 predictions with the ground truth values of AGB, which were similarly obtained via the field-based measurements
346 (provided by the regular tree-monitoring campaigns of ICOS [49] and WSL [46]) and Eq. 5.

347
348 The technique used to estimate model prediction error consisted of a nested cross-validation (NCV) scheme [85].
349 Following the NCV scheme, we divided the input dataset into 10 inner and 10 outer folds. In NCV, the results in the
350 inner folds report of the training performance, and they are used for model optimization, while the mean performance
351 on the outer folds is the one used for model evaluation. The model inspection technique used to evaluate predictors'
352 influence on the DBH regression results was the permutation importance method as proposed by Altmann et al.
353 (2010) [86]. The feature-elimination procedure consisted of eliminating progressively those predictors that presented
354 a negative mean importance, as they were considered harmful to the model's performance. The significance of the
355 enhancement in context-aware predictions and effect size was assessed using Wilcoxon signed-rank test [87] and
356 Cliff's Delta analysis [88], respectively.

357 | 3 | RESULTS

358 | 3.1 | Context Detection and Tree Assemblages

359 The analysis of spatial autocorrelation of tree height as function of incremental distance resulted in a maximum signif-
360 icance of clustering at a distance of 40 m. Figure 4 (a) shows the calculation of local Moran's index (I_i) of tree height
361 at different distance bands. Figure 4 (b) shows the standard score (i.e. z-score) of I_i obtained at each distance band,
362 resulting from comparing the observed I_i and the expected I_i under the tree height randomness assumption (details
363 included in Annex I). As a precaution, we ran context-aware regression experiments including also context features
364 retrieved at shorter (i.e. 20 m, 30 m) and larger (i.e. 50 m) distances than the optimal range (i.e. 40 m). The context
365 features retrieved at these distances (i.e. 20, 30, 40 and 50 m) which contributed to improve the predictions of DBH
366 were all included in the final regression models.

367 In Figure 5, panels a and b show the spatial distribution of tree assemblages calculated using either local Moran's
368 I_i or SL_i of tree height, respectively, at 40 m range. While both types of assemblages show similarities as regards
369 extent, morphometry and location, SL_i captures more local variability. This is not only due to a higher discretization
370 (5 groups in SL_i , vs. 3 groups in local Moran's I_i), but also to the fact that SL_i is insensitive to the variance in the
371 dataset beyond the range of its neighborhood, as explained in Section 2.3.

372
373 The morphometric analysis provided 40 additional features that were evaluated as potential predictors of DBH.
374 In Figure 6, panels a and b visualize the results of the morphometry analysis of tree assemblages defined by local
375 Moran's I_i and by SL_i , respectively. The circular barplots show the average magnitude as bar lengths, and the stan-
376 dard deviation as dots. Both mean and standard deviation values are shown as min-max scaled (across assemblage
377 types) to present all variables on the same radial axis and to ease visual comparison, i.e. for every morphometric
378 variable, the highest value is replaced by 1, the minimum is replaced by 0, and the intermediate values are linearly
379 interpolated between 0-1. It can be observed (Figure 6) that the morphometric variables follow very similar trends
380 when tree assemblages are defined based on local Moran's I_i or SL_i . However, an observed difference between SL_i
381 and local Moran's I_i was found in the heteroscedasticity of the morphometric variables calculated, where only in the
382 former case variance of all metrics scaled with magnitude.

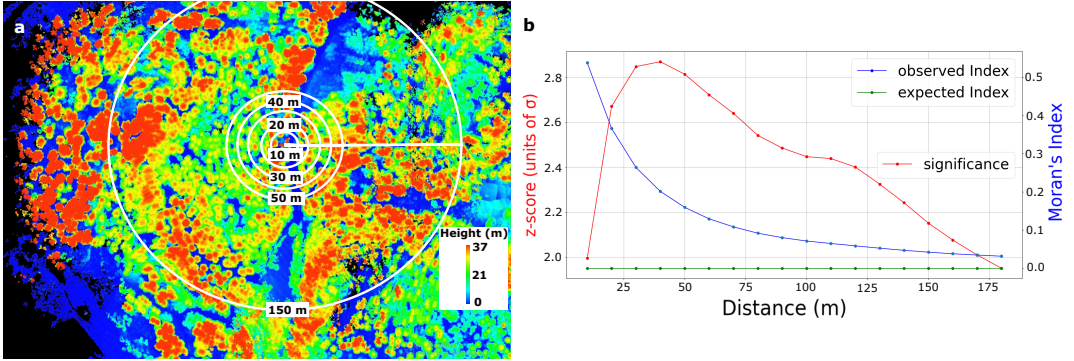


FIGURE 4 Context detection. **a:** Normalized point cloud data (PCD) scene colored by tree height overlaid with a selection of the appropriate radii for defining the neighboring context. **b:** Autocorrelation of tree height as function of distance. The red line shows the number of standard deviations (σ) that an observation is away from the expected value (under the assumption of heights being randomly distributed). The blue and green lines show the actually observed local Moran's Index and the expected value under randomness assumption, respectively.

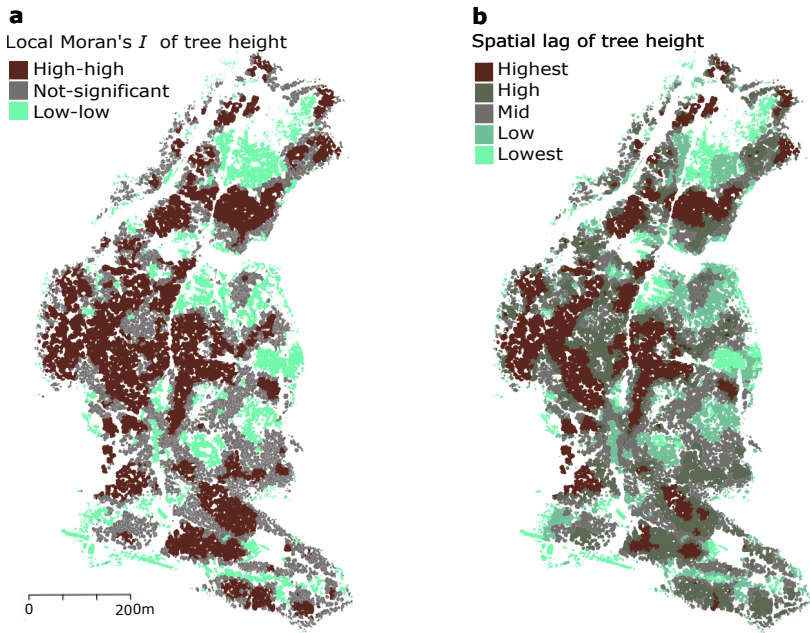


FIGURE 5 Tree assemblages defined by local similarity of tree height. **a:** Delineated according to local Moran's I_i of tree height. **b:** Delineated according to spatial lag of tree height.

383

384 While not for all variables a systematic trend was found, for several basic morphometric variables a linear positive
 385 correlation between them and SL_i was observed, as shown by the Pearson coefficient (ρ). This is the case for polygon

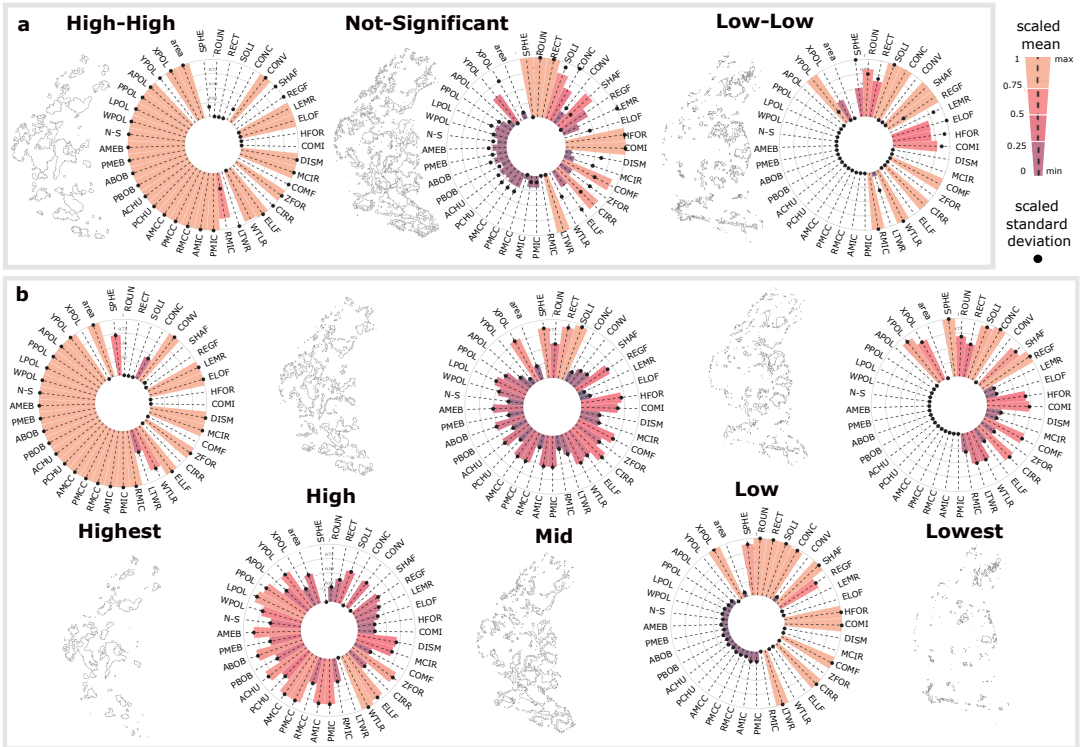


FIGURE 6 Morphometric analysis of tree assemblages grouped by (a) local Moran's I_i , and (b) by spatial lag of tree height. Bar length and color gradient represent the mean value, while black dots represent the standard deviation (SD) over all tree assemblages. Both mean and SD are scaled (min-max) to allow comparison of all metrics across assemblage types on the same axis—i.e. for every morphometric variable, the highest value of a certain assemblage type is replaced by 1, the minimum value is replaced by 0, and the intermediate values are linearly interpolated in between the range (0-1). YPOL: northing of centroid of the tree assemblage; XPOL: easting of centroid of the assemblage; APOL: area of polygon (P); N-S: defined as $|\sin(\text{azimuth})|$, shows the alignment of the main axis of P with the North-South direction; PPOL: perimeter of P; LPOL: major axis length (L) of P; WPOL: minor axis length (W) of P; ABOB: area of the bounding box fully containing P; PBOB: perimeter the bounding box fully containing P; AMEB: area of the minimum enclosing box fully containing P; PMEB: perimeter of the minimum enclosing box fully containing P; ACHU: area of containing hull ; PCHU: perimeter of convex hull fully containing P; AMCC: area of the minimum circumscribed circle (MCC); PMCC: perimeter of MCC; RMCC: radius of MCC; AMIC: area of maximum inscribed circle (MIC); PMIC: perimeter of MIC; perimeter of MCC; RMIC: radius of MCC; LTWR: length-to-width ratio [89]; WTLR: width-to-length ratio [90]; ELLF: ellipticity factor [91]; CIRR: circularity ratio [92]; ZFOR: Zavoianu's form factor [93]; COMF: compactness factor [74]; MCIR: Miller's circularity ratio [94]; DISM: dispersion measure [92]; COMI: complexity index [74]; HFOR: Horton's form factor [89]; ELOF: elongation ratio [95]; LEMR: lemniscate ratio [96]; REGF: regularity factor [91]; SHAF: shape factor [91]; CONV: convexity [97]; CONC: concavity [73]; SOLI: solidity [98]; RECT: rectangularity [99]; ROUN: roundness [97]; SPHE: sphericity [100]. Correlation coefficients of the most prominent variables are given in Annex III.

386 area ($\rho=0.95$), perimeter of polygon (PPOL; $\rho=0.98$) and radius of the minimum circumscribed circle (RMCC; $\rho=0.98$).
 387 Additionally, a positive correlation was found for some derived morphometric variables, namely: length-to-width ra-
 388 tio (LTWR; $\rho=0.75$) [89], circularity ratio (CIRR; $\rho=0.88$) [92], compactness factor (COMF; $\rho=0.89$) [74], dispersion

389 measure (DISM; $\rho=0.90$) [92], complexity index (COMI; $\rho=0.88$) [74], lemniscate ratio (LEMR; $\rho=0.81$) [96], regularity
 390 factor (REGF; $\rho=0.82$) [91], and concavity (CONC; $\rho=0.96$) [73]. Conversely, other morphometric variables showed a
 391 decreasing trend with increasing SL_i . A clearly negative correlation between SL_i and the following derived morpho-
 392 metric variables was found: Miller’s circularity ratio (MCIR; $\rho=-0.88$) [94], Horton’s form factor (HFOR; $\rho=-0.88$) [89],
 393 elongation factor (ELOF; $\rho=-0.83$) [95], shape factor (SHAF; $\rho=-0.95$) [91], rectangularity (RECT; $\rho=-0.85$) [99] and
 394 roundness (ROUN; $\rho=-0.69$) [97].

3.2 | AGB Predictions: Aware vs. Unaware of Local Context

396 Regression experiments including context-aware features improved predictions of DBH consistently (Figure 7, Ta-
 397 bles 1 and 2), resulting in enhanced tree-level AGB predictions via allometry (Eq. 5). All shallow learning methods
 398 improved prediction performance w.r.t R^2 , RMSE and MAE in both SP- and CP-datasets. For each pairwise compar-
 399 ison, the improvements were consistent, although the degree of prediction enhancement differed between the two
 400 datasets considered. Predictions in the CP-dataset observed a lower enhancement in comparison to predictions in
 401 the SP-dataset. For instance, RMSE was reduced by 9.1% (SP-dataset) vs. 4.0% (CP-dataset), and R^2 increased by
 402 3.5% (SP-dataset) vs. 3.2% (CP-dataset). This was expected, due to less variability in context in the CP-dataset, and
 403 may be indicative that capturing higher variability by the additional context features make them more effective.

404

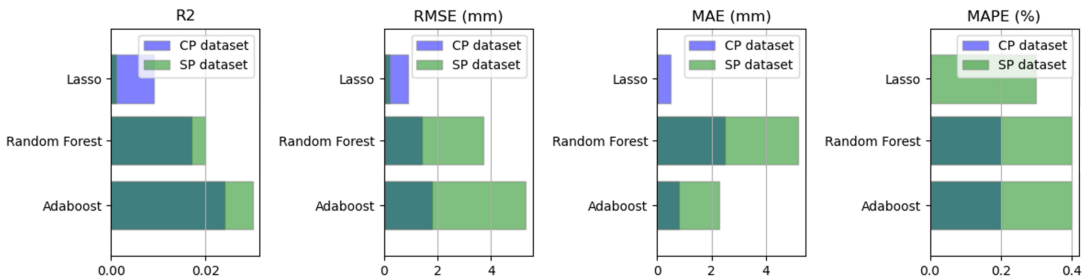


FIGURE 7 Enhancement of predictions of diameter at breast height per model type as a result of including context-based predictor variables (zero-reference corresponds to the prediction performance without including context-based predictors).

405 Figure 8 (a) shows the ground truth labels (i.e. field based estimates of AGB), which were derived from the field
 406 measurements and a species-specific allometric fit (i.e. Eq. 5). The central panel (b) shows the spatial distribution
 407 of residuals (i.e. $\epsilon = AGB_{ground,truth} - AGB_{prediction}$) of the AdaBoost context-aware regression results. The mean
 408 values converge towards zero (i.e. $\bar{\epsilon}_{SP} = 3.8$ kg, $\bar{\epsilon}_{CP} = -3.2$ kg), while the spread of the error distribution varies
 409 between SP and CP-datasets (i.e. $\sigma(\epsilon_{SP}) = 123$ kg, $\sigma(\epsilon_{CP}) = 140$ kg).

410

411 Figure 8 (b) shows the lack of high spatial autocorrelation of errors (i.e. low clustering of errors), indicating that
 412 predictions do not seem geographically biased. Figure 8 (c) displays the error distributions in both datasets. SP-errors
 413 show a unimodal distribution with a slight overestimation of DBH of -28 mm. CP-errors present a similar overesti-
 414 mation bias (-25 mm) with a bimodal distribution (the second mode is located at 25 mm of underestimation). The
 415 second mode of the bimodal pattern in the CP-dataset may correspond to the more frequent occurrence of larger
 416 trees, which tend to be underestimated (Figure 8, c, lower panels). It can be observed that, generally, smaller and

417 thinner trees tend to be slightly overestimated (i.e. in the first two quantiles) compared to the largest trees, which
 418 tend to be underestimated.

419

420 Figure 9 presents the analysis of the relative importance of all predictors considered in the context-aware DBH
 421 regression with the AdaBoost regression model (i.e. the best performing one). The analysis reveals that in both SP-
 422 and CP-datasets, the most important context-based predictors are the average heights of the 5, 10, and 15 nearest
 423 neighboring trees, outperforming some individual-tree metrics, such as the crown metrics.

424

425 TWI made a marginal contribution to enhanced predictions, which was less than that of any neighborhood met-
 426 ric. Moreover, although modest, TWI exhibited a greater impact on improved predictive performance at finer spatial
 427 resolutions in both datasets (Figure 9), whereas its contribution decreased at coarser resolutions (e.g. it did not sig-
 428 nificantly contribute as a predictor at 10 m² resolution). This observation may indicate that the spatial resolution at
 429 which TWI is most informative of individual tree height, is similar to the usual tree crown size (i.e. 2-5 m² resolution),
 430 while at a coarser spatial resolution its contribution as predictor becomes negligible.

TABLE 1 Results (on test set) of the SP-dataset, for each pairwise model comparison (aware vs. unaware of context features). Predictor variables are entirely LiDAR-derived; the target variable is diameter at breast-height (DBH, in mm). The values are presented as mean \pm standard deviation of the 10 outer CV folds of the nested scheme. One asterisk (*) marks results where the enhancement introduced by context-awareness is statistically significant with "small" size effect, while ** and *** mark "medium" and "large" size effect, respectively. The best results are shown in bold.

Regression model	R ²	RMSE (mm)	MAE (mm)	MAPE (%)
AdaBoost (unaware)	0.830 \pm 0.05	58.0 \pm 9.0	43.3 \pm 4.4	19.1 \pm 1.9
AdaBoost (aware)	0.860 \pm 0.03 ***	52.7 \pm 5.3 ***	41.0 \pm 3.1 **	19.5 \pm 1.7
Random Forest (unaware)	0.818 \pm 0.04	60.2 \pm 7.3	46.8 \pm 4.5	22.8 \pm 5.8
Random Forest (aware)	0.838 \pm 0.05 *	56.5 \pm 9.2 *	41.6 \pm 5.4 ***	22.4 \pm 5.1
Lasso (unaware)	0.851 \pm 0.02	54.6 \pm 4.9	4.20 \pm 3.3	19.1 \pm 1.4
Lasso (aware)	0.852 \pm 0.02	54.4 \pm 4.9	4.17 \pm 3.5	18.8 \pm 1.7

TABLE 2 Results (on test set) of the CP-dataset, for each pairwise model comparison (aware vs. unaware of context features). The predictive variables are entirely LiDAR-derived; the target variable is diameter at breast-height (DBH, in mm). The values are presented as mean \pm standard deviation of the 10 outer CV folds of the nested scheme. One asterisk (*) marks results where the enhancement introduced by context-awareness is statistically significant with "small" size effect. The best results are shown in bold.

Regression model	R ²	RMSE (mm)	MAE (mm)	MAPE (%)
AdaBoost (unaware)	0.713 \pm 0.07	54.7 \pm 5.98	43.0 \pm 5.26	15.5 \pm 2.4
AdaBoost (aware)	0.737 \pm 0.05 *	52.9 \pm 5.28 *	42.2 \pm 4.43 *	15.7 \pm 3.1
Random Forest (unaware)	0.688 \pm 0.07	57.0 \pm 5.9	43.8 \pm 5.1	15.7 \pm 3.1
Random Forest (aware)	0.705 \pm 0.04	55.6 \pm 5.3	41.3 \pm 5.5 *	15.9 \pm 4.3
Lasso (unaware)	0.741 \pm 0.09	51.3 \pm 6.6	39.1 \pm 5.2	13.6 \pm 1.6
Lasso (aware)	0.750 \pm 0.08	50.4 \pm 5.9	38.6 \pm 4.1	13.6 \pm 1.1

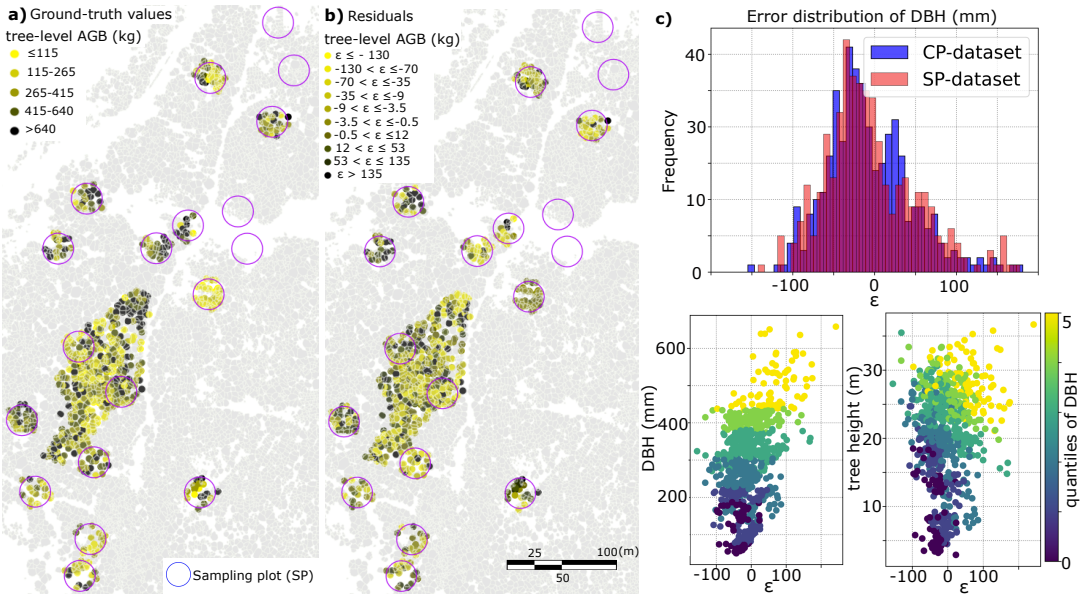


FIGURE 8 a: Spatial distribution of tree-level aboveground biomass (AGB) according to ground truth measurements. b: Spatial distribution of residuals ($\epsilon = AGB_{ground-truth} - AGB_{prediction}$) of AGB predictions with AdaBoost context-aware regression, grouped by quantiles (negative values indicate overestimation). The four empty SP-plots (and the southernmost one not included) correspond to areas where the quality of the UAV LiDAR data collection was compromised (Annex VI). c: Error distributions of diameter at breast-height (DBH) in sampling plot (SP) and control plot (CP) datasets. The two bottom-right panels show the error distribution of DBH (in x-axis) vs. field-measurements of DBH and tree height. The color scheme refers to the quantiles of each dataset separately, which are differently distributed (Annex V).

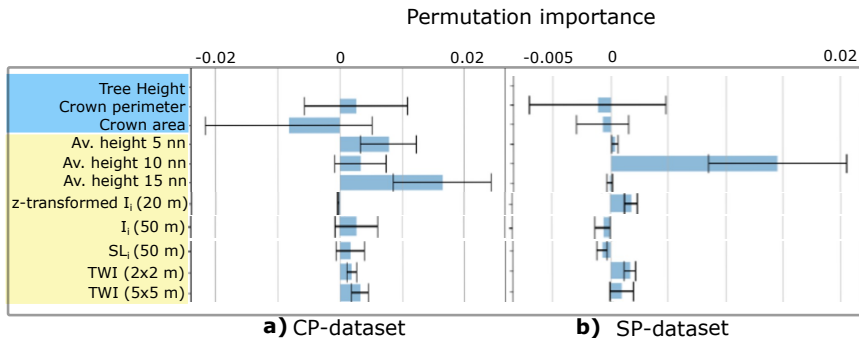


FIGURE 9 Inspection of predictors' permutation importance [86] in the AdaBoost regression experiment in context-aware conditions. The left panel (a) shows results in the control plot (CP) dataset, and the right panel (b) shows results in the sampling plot (SP) dataset. Bar length and error bar show the mean and standard deviation of a predictor's importance, respectively. Predictors highlighted in blue are individual tree traits; predictors highlighted in yellow are context-based. In both datasets, it can be noted how the average heights of the 5-15 nearest neighbors (nn) stand out as the strongest predictors, outperforming crown perimeter and crown area. In both plots (a and b), individual tree height (with importance: 0.85 in CP-dataset; 1.3 in SP-dataset) has been removed to facilitate visual comparison of the remaining predictors. Only the 11 most significant predictors are included; an extended figure is shown in Annex VII.

4 | DISCUSSION

4.1 | Enhancement of Tree-Level AGB Prediction

This study presents a method to enhance tree-level AGB estimates for coniferous forests using UAV LiDAR surveying and context-aware shallow learning regression methods. Our findings are consistent with established context learning literature [35, 36, 37, 38, 39, 40], remote sensing trait mapping studies [16, 34], and methodological advances on forest modelling—namely, NLME methods [17, 18] and competition-based studies [19, 20, 21]. We further extend this approach to a fully integrated UAV LiDAR framework. The pairwise comparison of twin methods consistently showed that context-aware regressions outperformed context-unaware regressions across models (except for Lasso in the SP-dataset, where performance virtually stagnated), and in no case adding context information became detrimental. This finding may indicate that gradients in tree heights across the ecosystem proxy for hidden environmental and biotic mechanisms (e.g. windstorm disturbance, nutrient and soil moisture abundance, light harvesting competition) [101, 102] that influence tree growth, and can therefore be leveraged to enhance predictions of AGB at the single tree level. The results showed a consistently improved performance in AGB prediction when including context. The improvements were tested as statistically significant in four of the six pairwise experiments, with size effect raging from small to large (Tables 1 and 2).

The accuracy enhancement gained from including context-aware features in the regression experiments varied between the two datasets considered (i.e. SP-trees and CP-trees). Context-aware regressions of DBH in SP-trees experienced greater enhancement than in CP-trees. This is consistent with the fact that the CP-dataset contains less variability of context, since it is a locally clustered and more homogeneous dataset, while the SP-dataset includes more variability in context features (Figure 2, b). The investigated Norway spruce forest presents a heterogeneous landscape, where the distribution of tree heights varies in space (Figure 5). Hence, the UAV LiDAR survey gives rise to a non-homogeneous dataset [62], which is a non-trivial question in automated tree phenotyping and functional trait mapping with ML methods [30, 34]. As SP-trees are grouped in scattered plots across the forest, their spatial distribution spans hundreds of meters, making them subject to a more diverse context than the very local CP-dataset.

4.2 | The Role of Neighboring Context in AGB Prediction Performance

Most shallow learning models achieved enhanced predictions when contextual information was included, with results consistently showing no deterioration (Tables 1 and 2). The average heights of the 10 and 15 nearest neighbors were the most important context based predictors for SP- and CP-trees, respectively (Figure 9). Moreover, the degree of local similarity of tree height (i.e. SL_i , local Moran's I_i) was most important and, to a lesser extent, the LiDAR-based TWI, indicating that although TWI may be a good predictor of tree growth [71], the neighborhood information resulted more useful significant, which lies in agreement with previous literature [23]. In contrast, including features informing about neighbor dissimilarity, such as local outliers of tree height detected using Local Outlier Factor [60] and Isolation Forest [61] algorithms did not result in enhanced predictions (thus not shown here). We hypothesize that metrics containing information about the degree of local similarity may reveal the combined effect of ecological processes that are specific to the immediate neighboring context. In contrast, metrics that proxy for dissimilarity do not help to uncover such processes, although they remain useful in detecting outstanding trees (i.e. local outliers).

Context-based features at closer distances generally showed larger predictive power but also larger variance (as

471 less neighboring trees were computed). For instance, the p-value of Local Moran's I_i at a 20 m range in the CP-dataset
472 has an average positive effect but is not a stable predictor (Figure 9, a). This can be observed in the general trend of
473 larger standard deviations in the permutation importance of predictors retrieved at short ranges than at greater dis-
474 tances (Annex VII). In accordance with competition-based studies [19, 20, 21], we observe that the strongest context-
475 based predictors are those retrieved from the immediate neighboring trees in both datasets, i.e. the average height
476 of 5, 10 and 15 nearest neighbors. However, our method additionally allows to compare the relative importance of
477 competition-derived metrics and other context-based metrics operating at larger scales. For instance, in Figure 9 (a)
478 it is shown that local Moran's I_i retrieved at a 50 m range is comparable in importance to the average height of the
479 closest 10 neighboring trees. A general difference observed between the CP and the SP-datasets is that the predictors'
480 importances in the CP-dataset fluctuate more (i.e. larger standard deviations). Further, in the SP-dataset, predictors
481 rarely become negative and if they do, it is to a lesser extent. Including morphometric variables calculated from the
482 tree assemblages (shown in Figure 6) in the regression experiments did not result in improved predictions of DBH
483 and therefore were not included in the final modelling of DBH.

484
485 Considering context metrics to enhance estimates of DBH at the individual tree level in coniferous forests has
486 been suggested in seminal works [25, 103] and been adopted subsequently for various applications in forest re-
487 search [24, 26, 21]. Moreover, recent investigations on tree morphology and productivity in coniferous forests [19, 20]
488 have motivated the further development of competition-aware approaches to improve the prediction accuracy of in-
489 dividual tree traits (e.g. growth), leveraging tree canopy metrics.

490
491 In forest biomass research, a commonly recognized approach is calibrating regression models with plot-level met-
492 rics for predicting tree-level structural traits (e.g. plot-level random effects in NLME methods), which has been pointed
493 out as a methodological limitation [23]. Indeed, the results of such approaches are constrained by the artificially-
494 delineated plot size, and it has been observed that accuracy increases with a progressively larger plot size [16, 18].
495 Our method to select context based on the spatial autocorrelation of tree heights (Figure 4) may indicate the range
496 of saturation of such improvement (40 m in this research site). Furthermore, our results show that the variability and
497 extent of context determines its beneficial leverage for prediction of tree-level traits (e.g. DBH, AGB).

498
499 This study continues this line of work and sheds light on how the local spatial context can be defined and leveraged
500 in tree-level structural trait predictions (i.e. DBH), making a case for AGB estimates in a Norway spruce forest. The
501 analysis shows that there is an optimal range to computing neighborhood metrics. In the study case considered here,
502 this corresponded to a 40 m range distance, based on the spatial autocorrelation of tree heights. Further, we found that
503 the predictive power of context-based metrics is sensitive to context extent (i.e. the range at which such metrics are
504 calculated). This observation may indicate that defining context based on plot-level metrics retrieved from artificially
505 bounded units [16, 17, 18] may be seen as a constrained approach, as observed previously [23, 104]. Likewise, in
506 the light of this observation, and in line with recent studies [105], determining the significant contextual extent of
507 individual functional traits based on units of fixed size (e.g. pixel size) appears to be a suboptimal technique. Therefore,
508 future forest research would probably benefit from including context-awareness determined by spatial association of
509 tree traits, bearing in mind that context-detection is trait-dependent and may vary depending on dataset source—e.g.
510 spatial autocorrelation as a function of distance (Figure 4) is sensitive to CHM segmentation quality—and method
511 applied—e.g. delineation of tree assemblages varied slightly between local Moran's I_i , and SL_i , as we show in Figure
512 5.

513 Lastly, we note that optical remote sensing studies usually define the optimal scale of analysis as a trade-off

514 between the observational extent (i.e. area surveyed) and the unit resolution (i.e. pixel size) [105, 106]. Also, in eco-
515 logical research, it is common to subsample datasets using natural subregions based on ancillary ecological criteria (e.g.
516 ecoregions, conservation status) [107]. Conversely, here we defined the range of influence of context-based metrics
517 (i.e. the extent of tree neighborhoods) using a dataset-native approach, based entirely on the spatial association of
518 individual tree heights. This permitted us to determine the context of influence unhampered by the remote sensing
519 technique and not using external data sources. Furthermore, as local context was defined based on the spatial asso-
520 ciation of a real physical attribute (i.e. tree heights), and not defined by an artificially bounded unit (e.g. pixel size or
521 plot size) the resulting distance could be considered characteristic of the forest ecosystem.

522 4.3 | Tree Assemblages

523 The analysis of morphometric variables for different tree assemblages (Figure 6) permitted to examine whether trees—
524 grouped by local association of tree heights—persistently show different shapes at the group level, shedding light on
525 the relationship between context-based traits (e.g. concavity of a tree assemblage) and single-tree heights. This
526 analysis revealed certain patterns of trait convergence [108], which was specially remarkable for some metrics, which
527 showed a strong correlation with tree height (e.g. concavity [73] and length-to-width ratio [89]). Nevertheless, none of
528 the morphometric variables obtained from the tree assemblage analysis proved useful to improve predictions of DBH.

529
530 Remarkably, it was observed that tree assemblages delineated according to the spatial lag of tree height (i.e. SL_i ,
531 Figure 6, b) presented clear positive correlations with two-dimensional morphometric features at the tree assemblage
532 level. For instance, assemblages with higher trees (i.e. labeled as *Highest* according to SL_i , or *High-High* according to
533 local Moran's I_i) are consistently rounder, larger and more regular in shape. As visualized in Figure 6, SL_i correlates
534 positively with shape regularity [91], two-dimensional concavity [73], length-to-width ratio [89] and size, indicating
535 a consistent trait-convergence assembly pattern [108]. Higher trees seem to converge in most sheltered areas (i.e.
536 thalwegs and local sub-basins) so that tree assemblages with highest SL_i tend to adopt the morphological features of
537 the drainage network's shape (Annex III). Interpretation of this observation would go beyond the scope of this study.
538 However, it may indicate that both the shape and location of tree assemblages of different heights are conditioned
539 by underlying environmental and biotic driving mechanisms.

540
541 In the coniferous forest studied here, a significant degree of clustering of tree heights takes place (Figure 5, a),
542 while spatial gradients of tree height present preferential shapes and directions (Figure 5, b). These observations
543 indicate that there is tree-height convergence and a tendency toward optimal phenotype expression (i.e. maximum
544 growth performance) around the runoff drainage network (in Annex III). Higher trees are found in sheltered regions
545 and concave channels—which generally benefit from more frequent runoff events and deeper soils [109, 110]. This
546 may indicate that favorable environmental conditions (e.g. deeper soil, lower soil moisture recession rates, greater
547 availability of soil nutrients due to leaching) allow individuals to reach their optimal phenotype. Conversely, a lower SL_i
548 of tree height in more exposed terrain (e.g. ridges, hilltops) may indicate that environmental filtering (e.g. windstorm
549 disturbance) or a reduced competition for light could play a significant role in determining the location of low SL_i tree
550 assemblages (Annex III). Thus, the relatively reduced tree height in exposed areas could indicate a passive adaptation
551 of tree height to harsher environmental conditions [111], an active adaptation to higher light availability [101], a
552 limitation to tree growth caused by other local factors, such as lower soil depth or nutrients availability [1, 110], or
553 the effect of these factors combined. Nevertheless, we cannot provide an interpretation of such observations, as
554 shifts in the variance of functional traits across environmental gradients, such as gradients in the spatial patterns of

555 trait similarity, do not bring strong evidence of either biotic or environmental filtering on their own [112].

556 4.4 | Methods Applied and Limitations

557 We have aimed at preserving a fully-native UAV LiDAR approach, so that the applicability of the method proposed
558 is not compromised by lacking local ancillary data (e.g. conservation status, edaphic conditions), whose availability
559 may become a limiting factor in forest monitoring. We note that these findings are specific to the mountainous
560 Norway spruce forest considered here. Caution is advised when contemplating a direct application of this approach
561 to more complex canopy structures and terrains, such as those found in deciduous, multilayered or broadleaf forests.
562 The strength of our results is currently limited by the lack of replicates at different forest sites, so that we cannot
563 yet confirm these findings to be generally applicable to a wider range of forest types and canopy configurations.
564 Furthermore, the pre-processing tasks (marked * in Figure 3, Section 2.3) required as part of our experimental design,
565 simplifies the actual PCD scene representing the real forest scenario. This simplification hampers a fully-automated,
566 streamlined application, and case-specific considerations are still required. In sum, further research is needed to
567 evaluate the transferability of the method.

568 5 | CONCLUSIONS

569 This study introduces and evaluates a fully integrated UAV LiDAR method that utilizes context information to improve
570 the accuracy of AGB estimates of individual trees with shallow learning methods, making a case for a coniferous for-
571 est. The prediction performance demonstrated improvements in AGB prediction when incorporating context-aware
572 features. The exception was the Lasso model, which stagnated in one of the datasets considered (SP-dataset). Import-
573 antly, in no case did contextual features have a detrimental effect. The results show that the use of context-aware
574 features as predicting variables can substantially improve estimates of AGB in coniferous forests—i.e. the best per-
575 forming model showed a reduction of RMSE of 9.1 % and 4.0 %, and an increase in R^2 by 3.5 % and 3.2 %, in the SP-
576 and CP-dataset, respectively. For the best performing method (AdaBoost regression), the strongest context-based
577 predictors were the average heights of the nearest 5-15 neighboring trees. Features that provide information about
578 the tree neighborhood (e.g. SL_i , of tree height, average height of k-nearest trees) contain useful information which
579 can be leveraged by shallow learning methods to improve predictions of diameter at breast height, and aboveground
580 biomass. This finding may suggest that the information retrieved from the local context serves as a proxy for un-
581 derlying ecological mechanisms that exert influence on the individual tree aboveground biomass as a result of local
582 adaptations to microclimate, edaphic conditions and biotic factors. We conclude that the use of UAV LiDAR surveys
583 and the integration of the spatial associations of tree heights is an efficient approach to incorporate context and thus
584 enhance forest biomass surveying.

585 References

- 586 [1] Fatichi S, Pappas C, Zscheischler J, Leuzinger S. Modelling carbon sources and sinks in terrestrial vegetation. *New*
587 *Phytologist* 2019;221(2):652–668.
- 588 [2] Pörtner HO, Roberts DC, Adams H, Adler C, Aldunce P, Ali E, et al. Climate change 2022: Impacts, adaptation and
589 vulnerability. IPCC Geneva, Switzerland.; 2022.
- 590 [3] Gundersen P, Thybring EE, Nord-Larsen T, Vesterdal L, Nadelhoffer KJ, Johannsen VK. Old-growth forest carbon sinks
591 overestimated. *Nature* 2021;591(7851):E21–E23.

- 592 [4] Friedlingstein P, Jones MW, O'sullivan M, Andrew RM, Hauck J, Peters GP, et al. Global carbon budget 2019. *Earth*
593 *System Science Data* 2019;11(4):1783–1838.
- 594 [5] Baccini A, Walker W, Carvalho L, Farina M, Sulla-Menashe D, Houghton R. Tropical forests are a net carbon source
595 based on aboveground measurements of gain and loss. *Science* 2017;358(6360):230–234.
- 596 [6] Duncanson L, Armston J, Disney M, Avitabile V, Barbier N, Calders K, et al. The importance of consistent global forest
597 aboveground biomass product validation. *Surveys in geophysics* 2019;40:979–999.
- 598 [7] Santini F, Kefauver SC, Resco de Dios V, Arais JL, Voltas J. Using unmanned aerial vehicle-based multispectral, RGB
599 and thermal imagery for phenotyping of forest genetic trials: A case study in *Pinus halepensis*. *Annals of Applied*
600 *Biology* 2019;174(2):262–276.
- 601 [8] Yao W, Krull J, Krzystek P, Heurich M. Sensitivity analysis of 3D individual tree detection from LiDAR point clouds of
602 temperate forests. *Forests* 2014;5(6):1122–1142.
- 603 [9] Dalponte M, Coomes DA. Tree-centric mapping of forest carbon density from airborne laser scanning and hyperspectral
604 data. *Methods in ecology and evolution* 2016;7(10):1236–1245.
- 605 [10] Kükenbrink D, Hueni A, Schneider FD, Damm A, Gastellu-Etchegorry JP, Schaepman ME, et al. Mapping the irradiance
606 field of a single tree: Quantifying vegetation-induced adjacency effects. *IEEE Transactions on Geoscience and Remote*
607 *Sensing* 2019;57(7):4994–5011.
- 608 [11] Cabo C, Ordóñez C, López-Sánchez CA, Armesto J. Automatic dendrometry: Tree detection, tree height and diame-
609 ter estimation using terrestrial laser scanning. *International journal of applied earth observation and geoinformation*
610 2018;69:164–174.
- 611 [12] Kukkonen M, Maltamo M, Korhonen L, Packalen P. Multispectral airborne LiDAR data in the prediction of boreal tree
612 species composition. *IEEE Transactions on Geoscience and Remote Sensing* 2019;57(6):3462–3471.
- 613 [13] Bertness MD, Callaway R. Positive interactions in communities. *Trends in ecology & evolution* 1994;9(5):191–193.
- 614 [14] Maestre FT, Callaway RM, Valladares F, Lortie CJ. Refining the stress-gradient hypothesis for competition and facilita-
615 tion in plant communities. *Journal of ecology* 2009;97(2):199–205.
- 616 [15] Muscarella R, Messier J, Condit R, Hubbell SP, Svenning JC. Effects of biotic interactions on tropical tree performance
617 depend on abiotic conditions. *Ecology* 2018;99(12):2740–2750.
- 618 [16] Hao Y, Widagdo FRA, Liu X, Quan Y, Dong L, Li F. Individual tree diameter estimation in small-scale forest inventory
619 using UAV laser scanning. *Remote Sensing* 2020;13(1):24.
- 620 [17] Yang Z, Liu Q, Luo P, Ye Q, Sharma RP, Duan G, et al. Nonlinear mixed-effects height to crown base model based on both
621 airborne LiDAR and field datasets for *Picea crassifolia* Kom trees in northwest China. *Forest Ecology and Management*
622 2020;474:118323.
- 623 [18] Liu X, Hao Y, Widagdo FRA, Xie L, Dong L, Li F. Predicting height to crown base of *Larix olgensis* in Northeast China
624 Using UAV-LiDAR data and nonlinear mixed effects models. *Remote Sensing* 2021;13(9):1834.
- 625 [19] Sun S, Cao QV, Cao T. Evaluation of distance-independent competition indices in predicting tree survival and diameter
626 growth. *Canadian Journal of Forest Research* 2019;49(5):440–446.
- 627 [20] Zhang B, Sajjad S, Chen K, Zhou L, Zhang Y, Yong KK, et al. Predicting tree height-diameter relationship from relative
628 competition levels using quantile regression models for Chinese fir (*Cunninghamia lanceolata*) in Fujian province, China.
629 *Forests* 2020;11(2):183.
- 630 [21] Lo CS, Lin C. Growth-competition-based stem diameter and volume modeling for tree-level forest inventory using
631 airborne LiDAR data. *IEEE Transactions on Geoscience and Remote Sensing* 2012;51(4):2216–2226.

- 632 [22] Potvin C, Dutilleul P. Neighborhood effects and size-asymmetric competition in a tree plantation varying in diversity. *Ecology* 2009;90(2):321–327.
633
- 634 [23] Ratcliffe S, Holzwarth F, Nadrowski K, Levick S, Wirth C. Tree neighbourhood matters—Tree species composition drives
635 diversity–productivity patterns in a near-natural beech forest. *Forest Ecology and Management* 2015;335:225–234.
- 636 [24] Andersen HE, McGaughey RJ, Reutebuch SE. Estimating forest canopy fuel parameters using LIDAR data. *Remote
637 sensing of Environment* 2005;94(4):441–449.
- 638 [25] Næsset E, Økland T. Estimating tree height and tree crown properties using airborne scanning laser in a boreal nature
639 reserve. *Remote Sensing of Environment* 2002;79(1):105–115.
- 640 [26] Rijal B, Weiskittel AR, Kershaw Jr JA. Development of height to crown base models for thirteen tree species of the
641 North American Acadian Region. *The Forestry Chronicle* 2012;88(1):60–73.
- 642 [27] Antonio N, Tome M, Tome J, Soares P, Fontes L. Effect of tree, stand, and site variables on the allometry of *Eucalyptus
643 globulus* tree biomass. *Canadian Journal of Forest Research* 2007;37(5):895–906.
- 644 [28] Hyyppä E, Yu X, Kaartinen H, Hakala T, Kukko A, Vastaranta M, et al. Comparison of backpack, handheld, under-canopy
645 UAV, and above-canopy UAV laser scanning for field reference data collection in boreal forests. *Remote Sensing*
646 2020;12(20):3327.
- 647 [29] Li N, Ho CP, Xue J, Lim LW, Chen G, Fu YH, et al. A Progress Review on Solid-State LiDAR and Nanophotonics-Based
648 LiDAR Sensors. *Laser & Photonics Reviews* 2022;16(11):2100511.
- 649 [30] Oehmcke S, Li L, Revenga JC, Nord-Larsen T, Trepekli K, Gieseke F, et al. Deep learning based 3D point cloud regres-
650 sion for estimating forest biomass. In: *Proceedings of the 30th International Conference on Advances in Geographic
651 Information Systems*; 2022. p. 1–4.
- 652 [31] Réjou-Méchain M, Barbier N, Couteron P, Ploton P, Vincent G, Herold M, et al. Upscaling forest biomass from field to
653 satellite measurements: sources of errors and ways to reduce them. *Surveys in Geophysics* 2019;40(4):881–911.
- 654 [32] Xu D, Wang H, Xu W, Luan Z, Xu X. LiDAR applications to estimate forest biomass at individual tree scale: Opportunities,
655 challenges and future perspectives. *Forests* 2021;12(5):550.
- 656 [33] Biging GS, Dobbertin M. Evaluation of competition indices in individual tree growth models. *Forest science*
657 1995;41(2):360–377.
- 658 [34] Schiefer F, Kattenborn T, Frick A, Frey J, Schall P, Koch B, et al. Mapping forest tree species in high resolution UAV-based
659 RGB-imagery by means of convolutional neural networks. *ISPRS Journal of Photogrammetry and Remote Sensing*
660 2020;170:205–215.
- 661 [35] Marques O, Barenholtz E, Charvillat V. Context modeling in computer vision: techniques, implications, and applications.
662 *Multimedia Tools and Applications* 2011;51:303–339.
- 663 [36] Zhao R, Ouyang W, Li H, Wang X. Saliency Detection by Multi-Context Deep Learning. In: *Proceedings of the IEEE
664 Conference on Computer Vision and Pattern Recognition (CVPR)*; 2015. p. 1265–1274.
- 665 [37] Chu HJ, Wu CF, Lin YP. Incorporating spatial autocorrelation with neural networks in empirical land-use change models.
666 *Environment and Planning B: Planning and Design* 2013;40(3):384–404.
- 667 [38] Luo W, Li Y, Urtasun R, Zemel R. Understanding the effective receptive field in deep convolutional neural networks.
668 *Advances in neural information processing systems* 2016;29.
- 669 [39] Yang W, Tan RT, Feng J, Liu J, Guo Z, Yan S. Deep joint rain detection and removal from a single image. In: *Proceedings
670 of the IEEE conference on computer vision and pattern recognition*; 2017. p. 1357–1366.

- 671 [40] Liu YF, Jaw DW, Huang SC, Hwang JN. DesnowNet: Context-aware deep network for snow removal. *IEEE Transactions*
672 *on Image Processing* 2018;27(6):3064–3073.
- 673 [41] Mittal S, Sharma I, Kumar A, et al. Comparative Analysis of Shallow Learning and Deep Learning. In: *2023 International*
674 *Conference on Next Generation Electronics (NEleX) IEEE; 2023. p. 1–8.*
- 675 [42] Jafari F, Moradi K, Shafiee Q. Shallow learning vs. deep learning in engineering applications. In: *Shallow Learning vs.*
676 *Deep Learning: A Practical Guide for Machine Learning Solutions Springer; 2024.p. 29–76.*
- 677 [43] Heiskanen J, C B, N B, C C, H C, B G, et al. The Integrated Carbon Observation System in Europe. *Bulletin of the*
678 *American Meteorological Society* 2022;103(3):E855–E872.
- 679 [44] Juszczak T. Voluntary National report to UNF1 from Switzerland. United Nations, Department of Economic and Social
680 *Affairs - Forests; 2019.*
- 681 [45] Burri S. Long-Term Environmental Research–The Davos-Seehornwald Site. *ETH Zurich Research collection* 2019;.
- 682 [46] WSL. Long-term Forest Ecosystem Research (WSL); 2023.
- 683 [47] TreeNet. Biological drought and growth indicator network; 2023.
- 684 [48] ETH-Zurich. Biological drought and growth indicator network; 2023.
- 685 [49] ICOS. Integrated Carbon Observation System; 2023.
- 686 [50] ICP-Forest. International Co-operative Programme on Assessment and Monitoring of Air Pollution Effects on Forests;
687 2023.
- 688 [51] eLTER. Integrated European Long-Term Ecosystem, critical zone and socio-ecological Research; 2023.
- 689 [52] Revenga JC, Trepikli K, Oehmcke S, Jensen R, Li L, Igel C, et al. Above-Ground Biomass Prediction for Croplands at a
690 *Sub-Meter Resolution Using UAV–LiDAR and Machine Learning Methods. Remote Sensing* 2022;14(16):3912.
- 691 [53] Davidson L, Mills J, Haynes I, Augarde C, Bryan P, Douglas M. Airborne to UAS LiDAR: An analysis of UAS LiDAR
692 *ground control targets. ISPRS Geospatial Week* 2019;.
- 693 [54] Swiss Federal Institute for Forest S, (WSL) LR. Methods of the Sanasilva Inventory; 2023.
- 694 [55] Hunziker S, Begert M, Scherrer SC, Rigling A, Gessler A. Below average midsummer to early autumn precipitation
695 *evolved into the main driver of sudden Scots pine vitality decline in the Swiss Rhône valley. Frontiers in Forests and*
696 *Global Change* 2022;p. 103.
- 697 [56] ICOS-ETC. Instruction on ancillary vegetation measurements in forest; 2023.
- 698 [57] Chen Q GP Baldocchi D, M K. Isolating Individual Trees in a Savanna Woodland Using Small Footprint Lidar Data. In:
699 *Photogrammetric Engineering and Remote Sensing, 72(8): 923-932; 2006. p. 923–932.*
- 700 [58] Anselin L. Local indicators of spatial association–LISA. *Geographical analysis* 1995;27(2):93–115.
- 701 [59] Anselin L, Rey SJ. Perspectives on spatial data analysis. In: *Perspectives on spatial data analysis Springer; 2010.p.*
702 *1–20.*
- 703 [60] Breunig MM, Kriegel HP, Ng RT, Sander J. LOF: identifying density-based local outliers. In: *Proceedings of the 2000*
704 *ACM SIGMOD international conference on Management of data; 2000. p. 93–104.*
- 705 [61] Liu FT, Ting KM, Zhou ZH. Isolation forest. In: *2008 eighth IEEE international conference on data mining IEEE; 2008.*
706 *p. 413–422.*

- 707 [62] Da Silva BC, Basso EW, Bazzan AL, Engel PM. Dealing with non-stationary environments using context detection. In:
708 Proceedings of the 23rd international conference on Machine learning; 2006. p. 217–224.
- 709 [63] Fu WJ, Jiang PK, Zhou GM, Zhao KL. Using Moran's I and GIS to study the spatial pattern of forest litter carbon density
710 in a subtropical region of southeastern China. *Biogeosciences* 2014;11(8):2401–2409.
- 711 [64] Anselin L, Syabri I, Kho Y. GeoDa: an introduction to spatial data analysis. In: *Handbook of applied spatial analysis:
712 Software tools, methods and applications* Springer; 2009.p. 73–89.
- 713 [65] Cressie N. *Statistics for spatial data*. John Wiley & Sons; 2015.
- 714 [66] Getis A, Ord JK. The analysis of spatial association by use of distance statistics. In: *Perspectives on spatial data analysis
715 Springer*; 2010.p. 127–145.
- 716 [67] Westerholt R, Resch B, Mocnik FB, Hoffmeister D. A statistical test on the local effects of spatially structured variance.
717 *International Journal of Geographical Information Science* 2018;32(3):571–600.
- 718 [68] Hastie TJ. *Generalized additive models*. In: *Statistical models in S* Routledge; 2017.p. 249–307.
- 719 [69] Anselin L, et al. *Spatial econometrics. A companion to theoretical econometrics* 2001;310330.
- 720 [70] Beven KJ, Kirkby MJ. A physically based, variable contributing area model of basin hydrology/Un modèle à base
721 physique de zone d'appel variable de l'hydrologie du bassin versant. *Hydrological sciences journal* 1979;24(1):43–69.
- 722 [71] Mohamedou C, Tokola T, Eerikäinen K. LiDAR-based TWI and terrain attributes in improving parametric predictor for
723 tree growth in southeast Finland. *International journal of applied earth observation and geoinformation* 2017;62:183–
724 191.
- 725 [72] ESRI. *ArcGis Pro: Implementation Guide*. Redlands, California; 2021, www.esri.com.
- 726 [73] Landini G. *Particles8 class: An ImageJ plugin for estimating various statistics of binary 8- connected particles.*; 2010.
- 727 [74] Güler C, Beyhan B, Tağa H. PolyMorph-2D: An open-source GIS plug-in for morphometric analysis of vector-based
728 2D polygon features. *Geomorphology* 2021;386:107755.
- 729 [75] Steiniger S, Blake L. *OpenJUMP software*; 2022.
- 730 [76] Freund Y, Schapire RE. A decision-theoretic generalization of on-line learning and an application to boosting. *Journal
731 of computer and system sciences* 1997;55(1):119–139.
- 732 [77] Friedman JH. Greedy function approximation: a gradient boosting machine. *Annals of statistics* 2001;p. 1189–1232.
- 733 [78] Schapire RE. Explaining adaboost. *Empirical Inference: Festschrift in Honor of Vladimir N Vapnik* 2013;p. 37–52.
- 734 [79] Tibshirani R. Regression shrinkage and selection via the lasso. *Journal of the Royal Statistical Society: Series B (Method-
735 ological)* 1996;58(1):267–288.
- 736 [80] Ho TK. Random decision forests. In: *Proceedings of 3rd international conference on document analysis and recognition,*
737 *vol. 1 IEEE*; 1995. p. 278–282.
- 738 [81] Vidaurre D, Bielza C, Larranaga P. A survey of L1 regression. *International Statistical Review* 2013;81(3):361–387.
- 739 [82] Demol M, Verbeeck H, Gielen B, Armston J, Burt A, Disney M, et al. Estimating forest above-ground biomass with
740 terrestrial laser scanning: Current status and future directions. *Methods in Ecology and Evolution* 2022;13(8):1628–
741 1639.
- 742 [83] Gryc V, Horáček P. Variability in density of spruce (*Picea abies* [L.] Karst.) wood with the presence of reaction wood.
743 *Journal of forest science* 2007;53(3):129–137.

- 744 [84] Scrinzi G, Galvagni D, Marzullo L. I nuovi modelli dendrometrici per la stima delle masse assestamentali in Provincia di
745 Trento. Provincia autonoma di Trento. Servizio foreste e fauna; 2010.
- 746 [85] Bates S, Hastie T, Tibshirani R. Cross-validation: what does it estimate and how well does it do it? arXiv preprint
747 arXiv:210400673 2021;.
- 748 [86] Altmann A, Toloşi L, Sander O, Lengauer T. Permutation importance: a corrected feature importance measure. *Bioin-*
749 *formatics* 2010;26(10):1340–1347.
- 750 [87] Wilcoxon F. Individual comparisons by ranking methods. Springer; 1992.
- 751 [88] Cliff N. Dominance statistics: Ordinal analyses to answer ordinal questions. *Psychological bulletin* 1993;114(3):494.
- 752 [89] Horton RE. Drainage-basin characteristics. *Transactions, American geophysical union* 1932;13(1):350–361.
- 753 [90] Zingg T. Beitrag zur schotteranalyse. PhD thesis, ETH Zurich; 1935.
- 754 [91] Buendia P, Soler C, Paolicchi F, Gago G, Urquieta B, Pérez-Sánchez F, et al. Morphometric characterization and
755 classification of alpaca sperm heads using the Sperm-Class Analyzer® computer-assisted system. *Theriogenology*
756 2002;57(4):1207–1218.
- 757 [92] Attneave F, Arnoult MD. The quantitative study of shape and pattern perception. *Psychological bulletin*
758 1956;53(6):452.
- 759 [93] Zăvoianu I. Morfometria bazinelor hidrografice. Editura Academiei Republicii Socialiste România; 1978.
- 760 [94] Miller VC. A QUANTITATIVE GEOMORPHIC STUDY OF DRAINAGE BASIN CHARACTERISTICS IN THE CLINCH
761 MOUNTAIN AREA VIRGINIA AND TENNESSEE. Columbia Univ New York; 1953.
- 762 [95] Schumm SA. Evolution of drainage systems and slopes in badlands at Perth Amboy, New Jersey. *Geological society of*
763 *America bulletin* 1956;67(5):597–646.
- 764 [96] Chorley RJ, Malm E Donald E, Pogorzelski HA. A new standard for estimating drainage basin shape. *American Journal*
765 *of Science* 1957;255:138–141.
- 766 [97] Horgan GW, Glasbey CA. Uses of digital image analysis in electrophoresis. *Electrophoresis* 1995;16(1):298–305.
- 767 [98] Zunic J, Rosin PL. A new convexity measure for polygons. *IEEE Transactions on Pattern Analysis and Machine Intelli-*
768 *gence* 2004;26(7):923–934.
- 769 [99] Rosin PL. Measuring rectangularity. *Machine Vision and Applications* 1999;11:191–196.
- 770 [100] Wadell H. Volume, shape, and roundness of quartz particles. *The Journal of Geology* 1935;43(3):250–280.
- 771 [101] Valladares F, Arrieta S, Aranda I, Lorenzo D, Sánchez-Gómez D, Tena D, et al. Shade tolerance, photoinhibition sensitivity
772 and phenotypic plasticity of *Ilex aquifolium* in continental Mediterranean sites. *Tree physiology* 2005;25(8):1041–
773 1052.
- 774 [102] Valladares F, Dobarro I, Sánchez-Gomez D, Pearcy RW. Photoinhibition and drought in Mediterranean woody saplings:
775 scaling effects and interactions in sun and shade phenotypes. *Journal of Experimental Botany* 2005;56(411):483–494.
- 776 [103] Naesset E. Determination of mean tree height of forest stands using airborne laser scanner data. *ISPRS Journal of*
777 *Photogrammetry and Remote sensing* 1997;52(2):49–56.
- 778 [104] Guillén-Escribà C, Schneider FD, Schmid B, Tedder A, Morsdorf F, Furrer R, et al. Remotely sensed between-individual
779 functional trait variation in a temperate forest. *Ecology and Evolution* 2021;11(16):10834–10867.

- 780 [105] Zheng Z, Zeng Y, Schuman MC, Jiang H, Schmid B, Schaepman ME, et al. Individual tree-based vs pixel-based ap-
781 proaches to mapping forest functional traits and diversity by remote sensing. *International Journal of Applied Earth*
782 *Observation and Geoinformation* 2022;114:103074.
- 783 [106] Ma X, Migliavacca M, Wirth C, Bohn FJ, Huth A, Richter R, et al. Monitoring plant functional diversity using the
784 reflectance and echo from space. *Remote Sensing* 2020;12(8):1248.
- 785 [107] Wang CJ, Zhang ZX, Wan JZ. Vulnerability of global forest ecoregions to future climate change. *Global Ecology and*
786 *Conservation* 2019;20:e00760.
- 787 [108] Pillar VD, Duarte LdS, Sosinski EE, Joner F. Discriminating trait-convergence and trait-divergence assembly patterns
788 in ecological community gradients. *Journal of Vegetation Science* 2009;20(2):334–348.
- 789 [109] Goebes P, Schmidt K, Seitz S, Both S, Bruelheide H, Erfmeier A, et al. The strength of soil-plant interactions under
790 forest is related to a Critical Soil Depth. *Scientific Reports* 2019;9(1):8635.
- 791 [110] Green JK, Keenan TF. The limits of forest carbon sequestration. *Science* 2022;376(6594):692–693.
- 792 [111] Valladares F, Gianoli E, Gómez JM. Ecological limits to plant phenotypic plasticity. *New phytologist* 2007;176(4):749–
793 763.
- 794 [112] Kraft NJ, Adler PB, Godoy O, James EC, Fuller S, Levine JM. Community assembly, coexistence and the environmental
795 filtering metaphor. *Functional ecology* 2015;29(5):592–599.